An Arc-Shaped Rotating Magnet Solution for 3D Localisation of a Drug Delivery Capsule Robot

Jaime Valls Miro[1*], Fredy Munoz[2], and Freyja Ivorie Miguel[1]

***Abstract*— A method to estimate the three-dimensional (3D) position of a capsule robot used to deliver drugs in the gastrointestinal tract is proposed in this paper. By exploiting the unique characteristics of the rotating magnetic field created by an array of tangentially magnetised arc-shaped permanent magnets (ASMs), and its analytical formulation, a capsule robot equipped with on-board Hall-effect sensors can measure the rotating magnetic fields created to infer its pose. Extensive validation results provided from a small rotating ASM experimental rig built to test the concept, and a complementary robotic setup for large scale testing are supplied. Given the proven homothetic transformations of magnetic fields, this work demonstrates with validated practical experimentation in a scaled-down rig (1/10), that a full rotation of the ASMs about one axis is sufficient to obtain a mean pose error < 10 mm in a magnetic system operating in scaled workspaces up to 250 mm, relevant for clinical use of capsule robots inside human bodies.**

I. Introduction

Untethered medical devices such as capsule robots are promising solutions for minimally invasive procedures [1]. These capsule robots are envisaged to include multiple on-board modules to achieve active locomotion [2], [3], biopsy [4], [5], and targeted drug delivery [6], [7] which will extend the diagnostic capabilities of existing wireless capsule endoscopes (WCEs, also known as "pill cams"). Actuation through magnetic fields has proven clinically feasible [8], [9] to be able to remotely activate and control prototypes of such on-board modules, and low-cost magnets are thus expected to continue to be integral in the next generation of WCEs.

Given their unbound nature, advances in the controllability of these micro-robots by integrating effective localisation modules capable of providing position and orientation of a capsule robot in the body, while remaining compatible with magnetic-actuated systems, are highly desirable. Although there have been significant efforts to develop localisation modules for capsule robots, none of them are commercial devices compatible with magnetic actuation [10]. An example uses gamma ray sources embedded in a capsule endoscope [11]. Similarly, several commercial devices such as the NDI Aurora System - and electromagnetic tracking (EM) device - are not amenable to magnetically actuated capsule robots because the embedded permanent magnets within the capsule robots can interfere with the EM tracking system [12].

[1] J. Valls Miro and F. Ivorie Miguel are with the Centre for Autonomous Systems, Faculty of Engineering and Information Technology, University of Technology Sydney, Australia jaime.vallsmiro@uts.edu.au, freyja.i.miguel@student.uts.edu.au

[2] F. Munozffmunozm09@gmail.com

[*] Corresponding Author

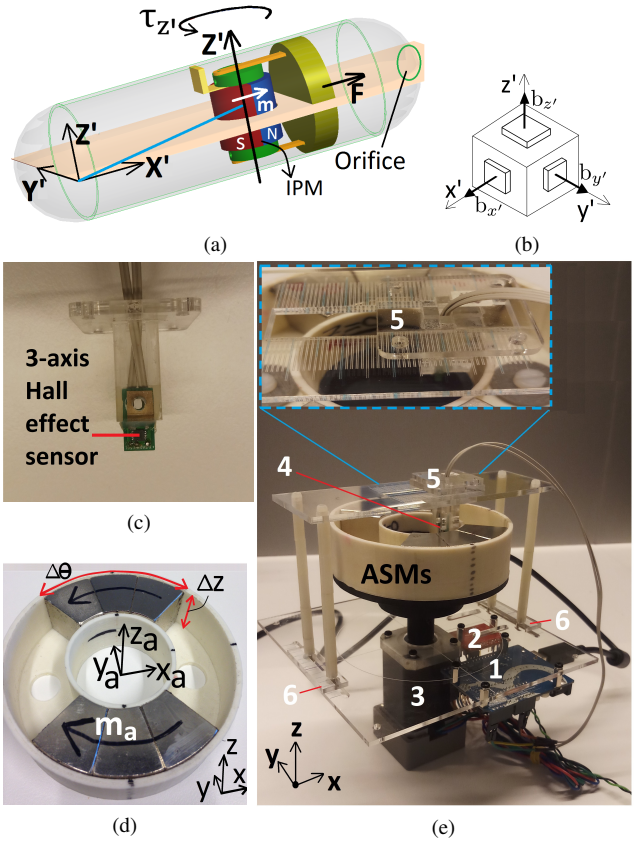

Fig. 1: (a) A capsule robot with an on-board drug release mechanism. (b) 3 Hall-effect sensor cube model visualisation. (c) 3-axis Hall-effect surface-mount sensor unit built for experimental testing. (d) Array of ASMs tangentially magnetised. (e) Rotating field experimental setup with: Arduino Uno (1), driver board (2), stepper motor (3), Hall-effect sensor unit (4) and sliders to position the sensor along the x- (5) and y-axis (6); inset shows a detail of the millimetric rulers laser engraved on acrylic to identify the desired poses.

MRI machines have also been used for either actuation [13], [14] or 6D localisation [15] of prototypes of medical devices, but there are no studies showing both functionalities working together in a capsule robot. From a technical perspective, it seems that an MRI machine could be used to achieve both functions simultaneously in capsule robots. However, an MRI machine would be an expensive solution which may not be easily adopted and widespread for clinical settings [16].

On the other hand, low-cost solutions have been developed to make use of the same magnetic field to actuate and detect the position and orientation of capsule robots [17]–[21]. For instance, rotating magnetic fields are used to estimate the 6D position and orientation of a capsule endoscope [17], while non-rotating magnetic fields generated by permanent magnets are used in [18] (in combination with an accelerometer) to estimate the 6D pose of a capsule robot. The functionality of these prototypes has been demonstrated with permanent magnets manipulated by robotic arms to achieve active locomotion of capsule robots. In these systems, Hall-effect sensors are fixed at predefined locations within the capsule robot. This minimises the interference of the magnetic field created by an internal permanent magnet (IPM) that is also fixed to the body of the capsule robot. Because these localisation methods are coupled with the locomotion of the capsule robot, they require the IPM and the Hall-effect sensors to be fixed to the capsule robot at all times. Therefore, they would be unsuitable for applications where the IPMs must move within the capsule such as a biopsy module [4], an anchoring mechanism [22] or an active drug delivery system (DDS) [6], [23].

Motivated by previous low-cost methods where the same magnetic dipole (i.e., a magnetic source that can be described by the point-dipole model) is used for active locomotion and localisation [17]–[20], and as an alternative to a potential MRI solution, a localisation module is proposed in this work that can integrate with a magnetic-actuated DDS for capsule robots by using multiple arc-shaped permanent magnets (ASMs) as the source for rotating magnetic fields. The novel scheme is necessary since the localisation methods proposed in the literature [17]–[21] are not compatible with a DDS for the following reasons: (a) the IPM and Hall-effect sensors used in [17]–[21] are fixed to the body of the capsule robot while for a DDS the IPM must freely rotate within the body of the capsule robot, (b) a geometry consisting of an array of ASMs rather than a single permanent magnet are proposed to generate the rotating magnetic field, and (c) the analytical models to estimate the magnetic fields (i.e., the point-dipole model used in [17], [21] or the analytical models for cylindrical permanent magnets used in [18]–[20]) are not accurate for the suggested ASMs actuation system.

Therefore, a custom 3D localisation method contingent on the rotating magnetic field generated by multiple ASMs has been conceived that, in conjunction with three on-board Hall-effect sensors, makes use of Coulombian-based models that can accurately describe the rotating magnetic field generated by ASMs [23]. This study is thus a step forward in the development of a localisation module envisioned to be compatible with a magnetic actuation system, as the same rotating magnetic field would be used to actuate a DDS and localise the capsule robot. The system has, in fact, been developed as a complement to methods previously developed for drug delivery using an array of ASMs [6] since for the same volume, multiple ASMs can generate higher magnetic torques than multiple magnetic dipoles, thus allowing further miniaturisation of the IPM [6].

TABLE I: Parameters of the ASMs

Parameter	Value
r_{in}	25.4 mm
r_{out}	50.8 mm
$\Delta\theta$	90^0
Δz	26.0 mm
$\|\mathbf{m_a}\|$	1.43 T

In this work, a novel method of rotating ASMs about one axis for 3D localisation is presented. It is demonstrated how rotating the ASMs about one axis is sufficient for 3D pose detection, instead of using three orthogonal axes for the rotation of an external magnetic dipole system, as in [17]. The external ASMs could be ultimately manipulated by robotic arms, or they can be mounted on a mobile platform similar to the one used in the Stereotaxis Corp. Niobe ES system. In this work, a mechatronic proof-of-concept scaled set-up with a stepper motor has been designed to validate the results experimentally.

The remainder of this paper is organised as follows. A motivating scenario for the use of the kind of DDS micro-robots advocated in this work is first presented in Section II. This is followed by a description of the capsule robot and the array of ASMs used in this work to generate the required rotating magnetic field, in Section III. The details of the algorithm for 3D localisation are presented in Section IV. Experimental results are examined in Section V. Finally, the significance of the results and future work are discussed in Section VI.

II. Motivation: Micro-robots for Medical Applications

An insight into the medical application that inspires the development of advanced capabilities for a robotic WCE can be succinctly described as follows: a capsule robot, illustrated by Fig. 1a, is first ingested by the patient. A clinician can broadly track its movements visually via an on-board imaging module, or a localisation module can track its precise position as it moves through the intestine. Once it reaches the target area within the body, an anchoring system can be deployed to limit the movement of the capsule. A localisation module can then be activated at this point if it was not being tracked to estimate the 3D location of the capsule accurately. Once the capsule is validated to be at the position of interest for medication, the on-board drug would be released (DDS). After the drug reservoir is emptied, the anchoring system would be deactivated, and the capsule could continue on its natural trajectory through the body.

This scenario requires compatible modules embedded within the capsule such as imaging, anchoring and localisation systems, to accurately control the drug release. An overall DDS consisting of a small IPM articulated with a slider-crank mechanism, and an array of ASMs surrounding

the patient's body to generate a rotating magnetic field to actively control the drug release module in the capsule has been proposed and experimentally validated in a lab setting [6]. This work proposes an additional compatible module to provide the 3D pose of the capsule robot.

III. ASMs and DDS Capsule Robot Preliminaries

Some characteristics of the ASM and reference frames are first provided as they will be used throughout the manuscript. Moreover, in terms of notation, bold lowercase font (**b**) and bold uppercase font (**B**) are used to denote vectors and matrices, respectively, whilst scalars are represented in lowercase fonts (b).

Each of the two tangentially magnetised ASMs proposed to prove the validity of the localisation solution in this work has an angular width of $\Delta\theta = 90^\circ$, which was obtained by putting together an array with three individual smaller segments, as shown in Fig. 1d. The parameters of the ASMs are summarised in Table I, where $\mathbf{m_a}$ refers to the tangential magnetisation vector of the ASM (depicted by a black arrow), and r_{in} and r_{out} denote the internal and external radii of the ASMs, respectively. These radii are taken with respect to the centre of the ASMs which coincides with the origin of the ASMs frame $X_aY_aZ_a$. The dimensions of the ASMs are chosen only for practical reasons, but the analysis and results are valid for any dimensions, as discussed in more detail in Section V-G.

To fully define a DDS capsule robot, three coordinate frames are required: the global frame XYZ can be arbitrarily chosen; the ASMs frame, $X_aY_aZ_a$, is attached to the centre of the ASMs as shown in Fig. 1d; and the robot capsule's frame, $X'Y'Z'$. The IPM can freely rotate about a central axis to operate the DDS mechanism, made to be parallel to the Z' axis for convenience, as shown in Fig. 1a. For the localisation problem, a 3-axis Hall-effect sensor is embedded at the origin of the capsule's frame to measure the three components of the ASM magnetic flux density perpendicular to each other, illustrated by the cuboid shown in Fig. 1b as in [20].

Furthermore, the following coordinate frames simplifications can be made for the 3D pose detection module: Z_a and Z are made to coincide, and therefore X, Y, X_a, Y_a all lie on the same plane. The capsule's frame, $X'Y'Z'$, is also aligned with the global frame for any capsule pose $\mathbf{p}_c = [x_c, y_c, z_c]$ (or, in cylindrical coordinates $\mathbf{p}_c = [r_c, \theta_c, z_c]$) within the region of operation. For the scaled ASM geometry used in the experimental work, this is defined by $0 \leq r \leq 24$ mm, $0^\circ \leq \theta \leq 359^\circ$ and $0 < z \leq 13$ mm (i.e., the upper section of the ASMs). The origin for $\mathbf{p}_c$ coincides with the origin of the global frame.

The rotating magnetic field used for localisation is generated as the ASMs are rotated about its Z_a axis by varying the angle between X_a and X, $0^\circ \leq \theta_{EPM} \leq 359^\circ$, in the counter-clockwise direction. The alignment of the capsule's frame with the global frame makes the proposed 3D localisation possible. If the capsule rotates about any of its 3 axes (as would be the likely case in the real application), the localisation system will be affected. In order to minimize this dependency on the alignment with the global frame, an on-board IMU sensor can be used to estimate the rotation of the capsule (as in [18]) or further manipulation of the remaining degrees of freedom of the ASMs may be required to collect additional magnetic field measurements (as in [17]). Detailed capsule design, or ASMs manipulation strategies are potentially viable strategies to overcome this issue that fall outside the scope of the work presented in this manuscript and are left for futre endeavours.

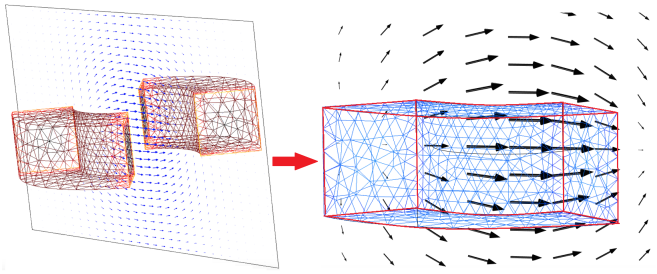

Fig. 2: The static **b** on the plane $Y = 0$ generated by our ASMs (on the left) and the inset (on the right) depicts the symmetry of **b** with respect to the X and Z axes.

The ensuing Section provides further details about the rotating magnetic field used for 3D pose detection.

IV. A Rotating Magneto-Mechatronic System for WCE Localisation

The three components of the static magnetic flux density, $\mathbf{b}(\mathbf{p})$, generated by ASMs tangentially magnetised can be calculated either by using the closed-form solutions presented in [24], or the Coulombian model which contains integral expressions that can be evaluated numerically as presented in [25]. The latter is the approach used in this paper as its accuracy has been validated for different dimensions of ASMs [23]. These analytical expressions can be employed to estimate the rotating magnetic field generated at any point **p** as the ASMs (shown in Fig. 1d) are rotated about the Z_a axis. These analytical models, which are valid for any ASMs dimensions, can be derived by firstly calculating the magnetic potential of a single ASM as follows:

$$\Phi(\mathbf{p}) = \frac{1}{4\pi\mu_0}\left(\sum_i \iint_{S_i} \frac{\mathbf{m_a}\cdot d\mathbf{S}_i}{\|\mathbf{p}-\mathbf{p}_i\|} + \iiint_{V_i} \frac{-\nabla\cdot\mathbf{m_a}}{\|\mathbf{p}-\mathbf{p}_i\|} dV_i\right) \quad (1)$$

where **p** and $\mathbf{p}_i$ represent an observation point and a point located on an ASM, respectively. The origin of these vectors coincides with the origin of the global frame XYZ. $\mathbf{S}_i$ and V_i represent a surface of an ASM and its volume, respectively. The permeability of free space is represented by μ_0. Secondly, the magnetic field of a single ASM, $\mathbf{h}(\mathbf{p})$, is obtained by calculating the gradient of the magnetic potential as follows:

$$\mathbf{h} = -\nabla\Phi(\mathbf{p}) \quad (2)$$

and in our case of two ASMs, the superposition principle has been used to obtain the total magnetic field $\mathbf{h}_t$ that is the sum of the two individual magnetic fields. Let $\mathbf{u}_r$, $\mathbf{u}_\theta$, $\mathbf{u}_z$

denote vectors of unit lengths expressing the magnetic field in cylindrical coordinates; $\mathbf{b}$ at any point $\mathbf{p}$ in cylindrical coordinates can thus be obtained by:

$$\mathbf{b}(\mathbf{p}) = \mu_0 \mathbf{h}_t = \mathrm{b}_r \mathbf{u}_r + \mathrm{b}_\theta \mathbf{u}_\theta + \mathrm{b}_z \mathbf{u}_z \tag{3}$$

where each component of $\mathbf{b}$ (i.e., b_r, b_θ and b_z) is described by an analytical expression that varies with $\mathbf{p}$. For instance, Fig. 2 shows $\mathbf{b}$ for $\mathbf{p}$ on the plane $\mathrm{Y} = 0$ which is obtained when $\theta_{\mathrm{EPM}} = 0$. The static $\mathbf{b}$ presents symmetries with respect to the X and Z axes as shown in Fig. 2 and therefore $\mathbf{b}(\mathbf{p})$ generated by our ASMs is not a one-to-one function. For this reason, $\mathbf{b}(\mathbf{p})$ is not an invertible function in the entire domain. Even when its domain is restricted to the upper section of the external magnetic system (i.e., $z \geq 0$), we find that $\mathbf{b}(\mathbf{p})$ is not invertible and does not provide sufficient information to uniquely determine the 3D pose of the capsule.

However, a rotating magnetic field can provide enough information to achieve 3D pose detection when the ASMs are made to rotate about a single axis (arbitrarily chosen here to be $\mathrm{Z_a}$). By varying θ_{EPM}, the direction of $\mathbf{p}_i$ and $\mathbf{S}_i$ will also vary according to (1). Thus, for each new value of θ_{EPM}, a new $\mathbf{b}$ can be estimated using (3). In this way, when the ASMs complete a full rotation - with increments of $\Delta\theta_{\mathrm{EPM}}$=1°, 360 readings are taken, each including the three components of $\mathbf{b}$. These readings are stored in a matrix $\mathbf{B}(\mathbf{p})$ of size 360x3 that represents the rotating magnetic flux density at the specific point $\mathbf{p}$. Therefore, $\mathbf{B}(\mathbf{p}) = (\mathbf{b}_k(\mathbf{p}))$ for k=1, 2, ..., 360. Note that the capsule is assumed to be anchored as the ASMs complete a full rotation, and therefore $\mathbf{p}$ does not vary. Given the slow movement of a capsule robot inside the body, this is effectively equiparable to a localisation control loop operating at a high rate.

An array $\mathbb{B}$ can then be created to store measurements of $\mathbf{B}(\mathbf{p})$ for each point within the operational region of the capsule robot. Increments of Δr=1 mm, $\Delta\theta$=1° and Δz=1 mm have been used in the practical settings explored in the next Section, although the resolution is predominantly dictated by the sensitivity of the Hall-effect sensors employed. For any unknown capsule pose, $\mathbf{p}_c = [r_c, \theta_c, z_c]$, the readings from the 3 Hall-effect sensors after a complete full rotation of the ASMs about its $\mathrm{Z_a}$ axis can be stored in a matrix $\mathbf{B}_m$ of size 360x3 that represents the rotating magnetic flux density measured at $\mathbf{p}_c$. Therefore, $\mathbf{B}_m = (\mathbf{b}_{mk})$ for k=1, 2, ..., 360. The 3D pose detection algorithm minimises the cost function $f(\mathbf{p}) = \|\mathbf{B}_m - \mathbf{B}(\mathbf{p})\|$ by searching through the lookup table $\mathbb{B}$. $f(\mathbf{p})$ is thus defined as follows:

$$f(\mathbf{p}) = \|\mathbf{B}_m - \mathbf{B}(\mathbf{p})\| = \sum_{k=1}^{360} \|\mathbf{b}_{mk} - \mathbf{b}_k(\mathbf{p})\| \tag{4}$$

whereby the solution renders the estimated capsule pose $\mathbf{p}$.

Because the rotating $\mathbf{B}(\mathbf{p})$ was observed to be symmetric with respect to the plane $\mathrm{Z} = 0$, and also for points located exactly on the plane $\mathrm{Z} = 0$ the inverse problem (the solution to (4)) reveals two results that are 180° out of phase, $\mathbf{p}$ had to be restricted to the upper section of the ASMs (i.e., $z > 0$) to guarantee that $\mathbf{B}(\mathbf{p})$ is a one-to-one function. This effectively halves the region of operation, yet it is conceivable that in practical terms the patient will lie on a table-bed surrounded by the external permanent magnet arrangement (as in the case in current MRI machine), in which case this will not be a limiting factor to its operation.

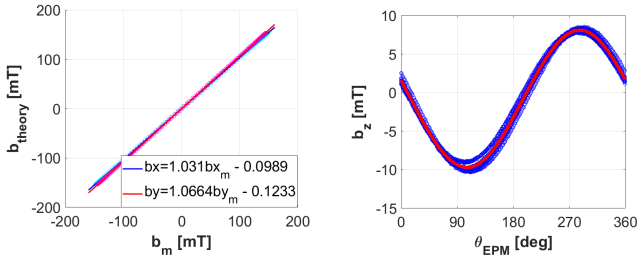

(a) (b)

Fig. 3: (a) Calibrated b_x and b_y (units in mT); $_m$ indicates measured, $_{theory}$ is derived from the analytical expression. (b) Averaged observed b_z deviation (in red) at the centre of the ASM, where SNR is lowest, used for calibration at a given angle of rotation θ_{EPM}.

V. Experimental Results

A. Preliminary Simulation

The validity of the scheme was first studied in a preliminary simulation, under idealistic conditions. An ASM workspace was defined by:

$$\begin{cases} 0.5 \leq r_c \leq 18.5 \text{ mm} & \Delta r_c = 6 \text{ mm} \\ 2.5^\circ \leq \theta_c \leq 332.5^\circ & \Delta\theta_c = 30^\circ \\ 0.5 \leq z_c \leq 12.5 \text{ mm} & \Delta z_c = 4 \text{ mm} \end{cases}$$

for a total of 192 points. The maximum position error for $\mathbf{p}_c$ was found to occur at the maximum range (r_c =18.5 mm, for any θ_c and any z_c), with an error of 0.72 mm. On the other hand, the position error was found to be minimum when $\mathbf{p}_c$ coincides exactly with one, and only one, $\mathbf{p}$ in the domain of the lookup table, where it showed $f = 0$. This is indicative of the uniqueness of the $\mathbf{B}(\mathbf{p})$ mapping approach.

B. Rotating ASM Mechatronic Setup

The components of the experimental setup are shown in Fig. 1e. A NEMA 17 bi-polar stepper motor with a 1.8° step angle (E-tech Industrial Co., China) was used to rotate the ASMs at increments of 1° by driving it from a Big Easy Driver stepper motor driver board, capable of 1/16 microstepping mode. A 3-axis linear Hall-effect sensor (ALS31300 with a range of ±0.2 T, Allegro MicroSystems, USA) was used to measure the rotating flux density. Its $[x_c, y_c, z_c]$ position was manually adjusted with sliders and millimetric rules laser engraved on acrylic sheets. An Arduino Uno controlled the stepper motor and read the Hall-effect sensor via $\mathrm{I^2C}$. Ten sensor readings were taken for a time window of 5 ms at each angular step. The average of the 10 readings was computed for each component of the static

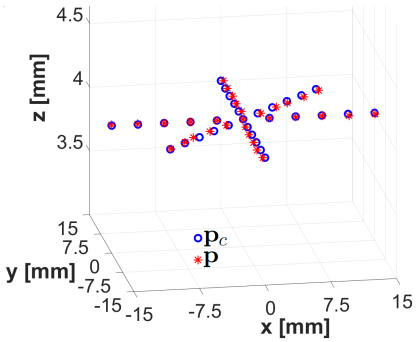

(a)

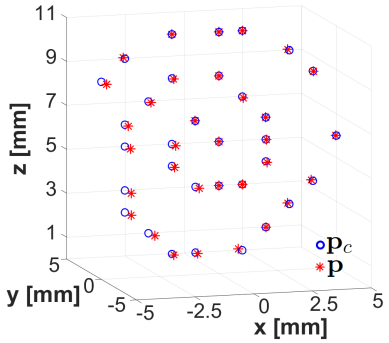

(b)

Fig. 4: (a) 3 linear paths on plane Z = 4 mm. (b) Spiral path on plane Y = 0. Ground truth (blue), estimated 3-D path (red).

TABLE II: Pose Estimation Error - Three Linear Paths

	$\mu + \sigma$	**worst**
x	0.01 ± 0.26 mm	0.69 mm
y	0.08 ± 0.25 mm	0.65 mm
z	0 ± 0 mm	0 mm
pose	0.30 ± 0.20 mm	0.69 mm

TABLE III: Pose Estimation Error - Spiral Path

	$\mu + \sigma$	**worst**
x	-0.01 ± 0.03 mm	0.08 mm
y	0.17 ± 0.30 mm	0.69 mm
z	0 ± 0 mm	0 mm
pose	0.25 ± 0.23 mm	0.70 mm

flux density. These averaged readings were collected until a full rotation of the ASMs was completed. The data was stored and later post-processed in MATLAB (Mathworks, Natick, MA, USA).

C. Sensor Calibration

The 3-axis Hall-effect sensor required calibration of the magnetic flux density components to account for individual sensor and ASM characteristics, and small inaccuracies in the alignment of the custom-design surface-mount sensing unit (Figure 1c). As shown in Fig. 3, a simple linear regression produced accurate corrections for b_x and b_y, whilst for b_z the average observed noise (shown in red) as the sensor moved along the Z axis from 1 to 10.5 mm, where SNR is at the lowest, was considered.

D. Pose Estimation Errors

The pose error was calculated as the distance between the ground truth of $\mathbf{p}_c$ and its estimated pose obtained by minimising (4). Three linear paths in a radiating, asterisk-like structure on a plane (Fig. 4 (a)) and a spiral path (Fig. 4 (b)), also on a plane, covering a large area of workspace were assessed. Each path was repeated 10 times to report the mean ± standard deviation and the maximum error. The three paths all lied on the plane Z = 4 mm and consisted of 31 points, defined by

$$\begin{cases} \text{-15 mm} \leq y_c \leq 15 \text{ mm} & x_c = 0, \Delta y_c = 3 \text{ mm} \\ \text{-15 mm} \leq x_c \leq 15 \text{ mm} & y_c = 0, \Delta x_c = 3 \text{ mm} \\ \text{-10 mm} \leq x_c \leq 10 \text{ mm} & x_c = y_c, \Delta x_c = 2 \text{ mm} \end{cases}$$

whereas the spiral path consisted of 34 points on the plane Y = 0. The pose errors along these paths are collected in Tables II and III. The maximum error of 0.70 mm occurred in the spiral path at $\mathbf{p}_c = [-4, 0, 3]$ mm (where the estimated pose was $\mathbf{p} = [x, y, z] = [-3.9, -0.7, 3]$ mm).

In terms of computational time, the proposed algorithm firstly computes $f(\mathbf{p})$ for all points in the entire domain. On average, it takes 20 seconds to then estimate the 3D pose for a new measurement. In terms of accuracy, it was found that $\mathbf{B}(\mathbf{p})$ tends to be close to $\mathbf{B}_m$ as $\mathbf{p}$ gets closer to $\mathbf{p}_c$. In fact, the position error can be further reduced by decreasing Δr, $\Delta\theta$ and Δz (thus increasing the look-up workspace resolution) at the expense of greater computational time. Because the rotating magnetic field is a one-to-one function (for $z > 0$), $f(\mathbf{p})$ could be computed until its value is less than a predetermined threshold, instead of doing so over the entire domain in the lookup table. Moreover, rather than searching over a lookup table, a Jacobian-based method [18] can also be used in which the optimisation of (4) would be guided by the gradient of $\mathbf{B}(\mathbf{p})$. These strategies are currently being explored and left as future work.

E. Robotic Arm Setup

Manual positioning of the sensor allowed greater fine tuning with the rotating ASM rig and sensor probe, and was thus preferred for early development and for smaller operations, yet proved to be impractical for testing at scale. Consequently, a 6 DoF Universal Robots UR3 (with an experimentally validated repeatability of ±0.1 mm) test rig was used to repeatedly position the sensor probe within the working volume, as shown by Fig. 5, and collect a larger series of random and structured set of points, illustrated in Fig. 5b, repeated 9 times. Unlike the case of the manual

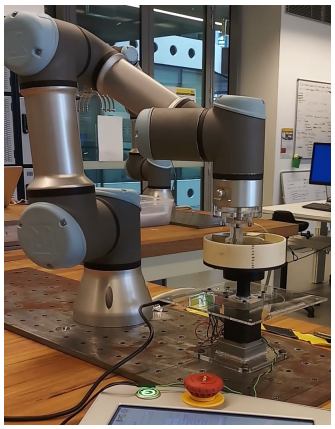

(a)

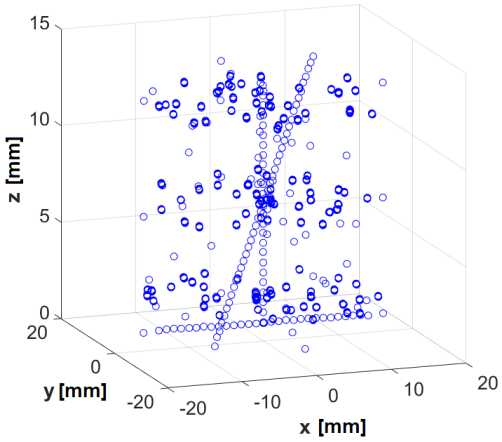

(b)

Fig. 5: (a) Testing rig with rotating ASM and robotic setup with UR3 manipulator. (b) Data points collected by UR3 (in mm).

TABLE IV: Pose Estimation Error - Robotic Arm Setup

	$\mu + \sigma$	**worst**
x	-0.001 $\pm$ 0.41 mm	1.14 mm
y	0.05 $\pm$ 0.43 mm	1.21 mm
z	-0.10 $\pm$ 0.38 mm	1.09 mm
pose	0.64 $\pm$ 0.31 mm	1.60 mm

paths examined, estimates are omitted to add clarity to the graph, otherwise is too cluttered given the large number of test points.

The position information published by the robot was used as ground truth to calculate errors for the 1,251 points with respect to the estimates fom the proposed lookup table locations, collected in Table IV. It can be observed how the errors are very small on average, although with somewhat larger uncertainty fluctuations and individual variability when compared to those obtained manually over the reduced set of points that conformed the linear and spiral paths, effectively equating to more or less double in size overall.

F. Sensitivity and SNR

The sensitivity of $\mathbf{B}$ to changes in $\mathbf{p}$ over the entire 3D region of operation, as well as the signal-to-noise ratio (SNR) to estimate how the pose error can vary as a function of $\mathbf{p}$, was also assessed. The former can be estimated by using the following approximation (finite-difference of $\mathbf{B}$):

$$\frac{\Delta \mathbf{B}}{\Delta \mathbf{p}} = \left[\frac{\Delta \mathbf{B}}{\Delta r} \frac{\Delta \mathbf{B}}{r \Delta \theta} \frac{\Delta \mathbf{B}}{\Delta z} \right] \tag{5}$$

with $\Delta \mathbf{B}$ defined as

$$\Delta \mathbf{B} = \|\mathbf{B}(\mathbf{p}_{j+1}) - \mathbf{B}(\mathbf{p}_j)\| = \sum_{k=1}^{360} \|\mathbf{b}_k(\mathbf{p}_{j+1}) - \mathbf{b}_k(\mathbf{p}_j)\| \tag{6}$$

and $\Delta \mathbf{p}$ representing the change in capsule's position from $\mathbf{p}_j$ to $\mathbf{p}_{j+1}$. Although Fig. 6 shows theoretical results for $\frac{\Delta \mathbf{B}}{\Delta \mathbf{p}}$ only at $\theta = 0^\circ$, the same results are found regardless of the value of θ. Thus, Fig. 6 effectively depicts $\frac{\Delta \mathbf{B}}{\Delta \mathbf{p}}$ for any point in the region of operation of the capsule robot. According to these results, the sensitivity of $\mathbf{B}$ (and consequently the SNR) decreases for points near the centre of the system and is improved as r and z increase.

The minimum (theoretical) value of $\frac{\Delta \mathbf{B}}{\Delta r}$ was found to be 117 mT/mm - when the capsule's position changes from $\mathbf{p}_j = [0,0,1]$ mm to $\mathbf{p}_{j+1} = [1,0,1]$ mm. The algorithm was sensitive to this small change in sensor's position (pose error 0.78 $\pm$ 0.38 mm and a maximum of 1.50 mm).

To validate experimentally, the 3-axis Hall-effect sensor was moved (with $\|\Delta \mathbf{p}_c\|$=1 mm) within the workspace, specifically following 8 paths $T_i, i = 1...8$ that mapped back onto the edges of the sensitivity SNR gradient surfaces

$$\begin{cases} T_1 = [0,0,z_c], T_2 = [1,0,z_c], & \\ T_3 = [15,0,z_c], T_4 = [16,0,z_c] & 1 \text{ mm} \leq z_c \leq 13 \text{ mm} \\ T_5 = [r_c,0,1], T_6 = [r_c,0,2], & \\ T_7 = [r_c,0,12], and T_8 = [r_c,0,13] & 1 \text{ mm} \leq r_c \leq 16 \text{ mm} \end{cases}$$

for a total of 116 points. For each T_i, 10 measurements were collected at each point, manually operating the rotating ASM rig for finer error control given the marginally more accurate restults obtained using the manual mechatronics ASM test-rig when compared to the robotic setup. The experimental results for $\frac{\Delta \mathbf{B}}{\Delta r_c}$ and $\frac{\Delta \mathbf{B}}{\Delta z_c}$ after applying (5) to each path T_i, are depicted in red over the theoretical results in Figs. 6a and 6b, respectively.

These results validate the theoretical predictions over the experimental ASM 3D region of operation. For all points in T_i, the distribution of pose errors was decidely small (0.27 $\pm$ 0.29 mm), very similar values to those previosuly reported experimentally with the linear and spiral paths. The maximum mean error of 1.67 mm occurred at $\mathbf{p}_c = [1,0,2]$

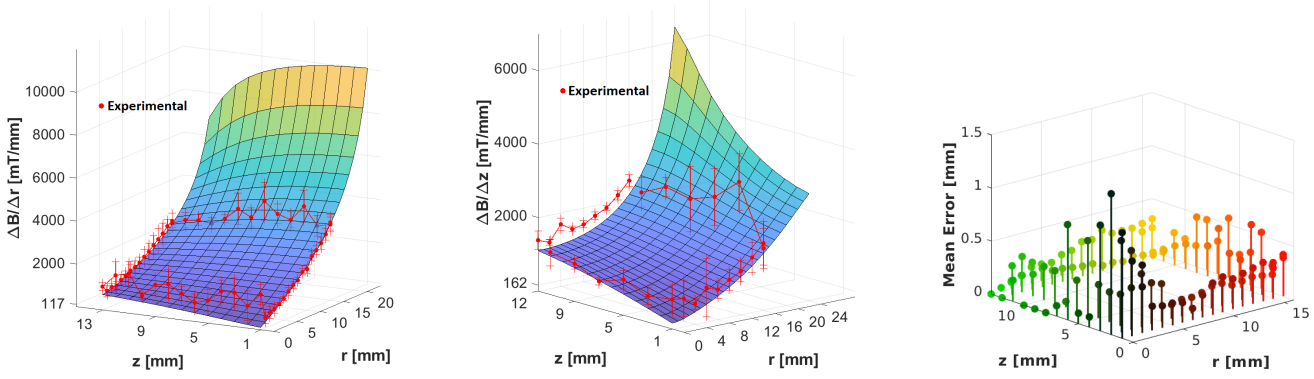

(a) (b) (c)

Fig. 6: Theoretical (coloured surface plot) and experimental (superimposed red dots) SNR analysis with $\frac{\Delta \mathbf{B}}{\Delta \mathbf{p}}$ with θ fixed at 0°. (a) $\frac{\Delta \mathbf{B}}{\Delta r}$. (b) $\frac{\Delta \mathbf{B}}{\Delta z}$. (c) Mean pose error for points along the 8 SNR test paths.

mm. It was observed (see Fig. 6c) how errors tended to increase around and beyond 1 mm for points near the centre of the rotating ASM system and decreased below 0.6-0.8 mm for points farther away from the centre. Hence, worse error conditions appear closer to those observed with the robotic set-up, gathered in Table IV. This can be likely attributed to the much larger cohort of test points acquired with the robot, where more disperse values are more likely to appear over the workspace. Since these small variations of $\mathbf{B}$ can be measured by commercially available Hall-effect sensors with increased sensitivity [17], [26] over the one used in the experimental tests, it can be concluded that an error bound of approx. 1.7 mm can be safely expected (for points near the centre of the system), and less than 1 mm error otherwise.

G. ASMs Scaling for Practical Applications

It has been previously shown that magnetic fields generated by permanent magnets are suitable for clinical use as the magnetic field scales homothetically [27]. This property, which is valid for any arc-shaped permanent magnet, has been further confirmed theoretically for any 3D point using FEM Comsol and the Coulombian model, and tested for a variety of factors [6], [23]. In these studies the 3D magnetic flux density in the entire 3D region of operation of the capsule robot was computed, obtaining the same 3D magnetic flux densities at the corresponding scaled positions, regardless of scaling factor. Moreover, it has been validated experimentally with a system of 4 ASMs [6] and up to 24 ASMs [28]. This implies that scaling up the proposed ASMs geometries by a factor s and measuring the magnetic field at the corresponding scaled position $s\mathbf{p}$ is equivalent to measuring the magnetic field generated by the unscaled ASMs at the position $\mathbf{p}$, and therefore (5) and (6) also scale homothetically.

Hence, when the dimensions of the ASMs are for example scaled up 10 times - as in this work (i.e. s=10, thus obtaining an operating distance of $10 \times \mathrm{r_{in}} = 250$ mm, more relevant for clinical use), the minimum $\Delta\mathbf{B}$ will remain 117 mT for an equivalent scaled pose change $s\Delta\mathbf{p} = 10 \times 1$ mm, i.e. from $\mathbf{p}_j = [0,0,10]$ mm to $\mathbf{p}_{j+1} = [10,0,10]$ mm. Consequently, the scaled-up ASM 3D system would be able to estimate a change in capsule's pose with a maximum error of approximately 17 mm (at the most critical point, near the origin of the system). At other points in the region of operation of the capsule robot, $\Delta\mathbf{B}$ has been shown to be greater than 117 mT, and so the position error can be expected to reduce accordingly to within a few millimetres (with a mean error value $<$10 mm).

This is a stepped improvement over other magnetic localisation work reported for magnetic capsules whereby rotation of a magnetic dipole about only one axis was found insufficient (with a mean pose error $>$26 mm at its best), and had to be actuated about its three orthogonal axes to achieve a mean pose error $<$10 mm [17]. Therefore, our 3D system shows promising results for future clinical applications. This localisation improvement is due to the highly non-uniform magnetic field generated by ASMs. Although both ASMs and magnetic dipoles generate non-uniform magnetic fields, the degree of non-uniformity has been proven to be higher for ASMs. This would naturally lead to higher SNR and lower localisation errors with ASMs. In fact, it has been shown with ASMs that the magnitude of the rotating magnetic field does not resemble an ellipse (as it is the case for a magnetic dipole) but varies uniquely in the 3D region of operation and generates signatures more complex than an ellipse [28]. This is what we exploit in this work on localisation.

It is important to note that strategic movements of the ASMs can increase the certainty in the capsule's pose by locating it within more sensitive regions, where $\Delta\mathbf{B}$ is greater. For example, radial movements of the ASMs' would incur higher SNR than ASMs' movements along the Z direction. Another way to improve the certainty in the detection of the capsule's pose is by using estimation filters such as particle [29] or Kalman filters [30]. The implementation of more advance estimators or the manipulation of the rotating ASMs with more flexible actuating units (e.g. a robotic arm or a mobile robotic platform) is left for future work.

VI. Conclusions and Future Work

A novel 3D localisation method that uses the 1D rotating magnetic field generated by multiple ASMs tangentially magnetised has been presented in this work. Exploiting the highly non-uniform rotating magnetic fields generated by ASMs, and a simple minimisation from a lookup table, the feasibility of this low-cost localisation approach has been demonstrated with an experimental rig. The method makes use of three on-board Hall-effect sensors and demonstrates that it is sufficient to rotate the ASMs about its Z_a axis to obtain a maximum pose error of 17 mm (with a mean value < 10 mm) in a scaled up system with dimensions useful for clinical applications. Extensive validation results are also provided from testing the assembled rotating ASM experimental rig on a robotic arm setup, indicating close agreement between the proposed models for localisation and the actual measured poses. This paper represents a step forward in the development of a localisation module that is envisioned to be compatible with industry-standard magnetic actuation systems to achieve targeted drug delivery in the digestive system. Future work includes the full integration of the magnetic-actuated drug delivery system with the proposed magnetic-based localisation module presented in this work and consideration for more advanced estimation algorithms. The implications to extend the methodology to full 6 DoF localisation are also being investigated.

References

[1] G. Ciuti, R. Caliò, D. Camboni, L. Neri, F. Bianchi, A. Arezzo, A. Koulaouzidis, S. Schostek, D. Stoyanov, C. M. Oddo, B. Magnani, A. Menciassi, M. Morino, M. O. Schurr, and P. Dario, "Frontiers of robotic endoscopic capsules: A review," *Journal of Micro-Bio Robotics*, vol. 11, no. 1, pp. 1–18, 2016.

[2] Z. J. Sun, B. Ye, Y. Qiu, X. G. Cheng, H. H. Zhang, and S. Liu, "Preliminary study of a legged capsule robot actuated wirelessly by magnetic torque," *IEEE Trans. on Magnetics*, vol. 58, no. 8, 2014.

[3] H. Zhou, G. Alici, T. D. Than, and W. Li, "Modeling and experimental investigation of rotational resistance of a spiral-type robotic capsule inside a real intestine," *IEEE/ASME Trans. on Mechatronics*, vol. 18, pp. 1555–1562, 2013.

[4] M. Simi, G. Gerboni, A. Menciassi, and P. Valdastri, "Magnetic torsion spring mechanism for a wireless biopsy capsule," *ASME Journal of Medical Devices*, vol. 7, no. 4, pp. 1–9, 2013.

[5] S. Yim, E. Gultepe, D. Gracias, and M. Sitti, "Biopsy using a magnetic capsule endoscope carrying, releasing and retrieving untethered micro-grippers," *IEEE Trans. on Biomedical Engineering*, vol. 61, no. 2, pp. 513–521, 2013.

[6] F. Munoz, G. Alici, and W. Li, "A magnetically actuated drug delivery system for robotic endoscopic capsules," *ASME Journal of Medical Devices*, vol. 10, no. 1, pp. 1–11, 2016.

[7] S. P. Woods and T. G. Constandinou, "Wireless capsule endoscope for targeted drug delivery: Mechanics and design considerations," *IEEE Trans. on Biomedical Engineering*, vol. 60, no. 4, pp. 945–953, 2013.

[8] Z. Liao, X. Duan, L. Xin, L. Bo, X. Wang, G. Xiao, L. Hu, S. Zhuang, and Z. Li, "Feasibility and safety of magnetic-controlled capsule endoscopy in examination of human stomach: A pilot study in healthy volunteers," *J. Intervent. Gastroent.*, vol. 2, no. 4, pp. 155–160, 2012.

[9] L. J. Sliker and G. Ciuti, "Flexible and capsule endoscopy for screening, diagnosis and treatment," *Expert Review of Medical Devices*, vol. 11, no. 6, pp. 649–666, 2014.

[10] T. D. Than, G. Alici, H. Zhou, and W. Li, "A review of localization systems for robotic endoscopic capsules," *IEEE Trans. on Biomedical Engineering*, vol. 59, no. 9, pp. 2387–2399, 2012.

[11] T. D. Than, G. Alici, S. Harvey, G. O'Keefe, H. Zhou, W. Li, T. Cook, and S. Alam-Fotias, "An effective localization method for robotic endoscopic capsules using multiple positron emission markers," *IEEE Trans. on Robotics*, vol. 30, no. 5, p. 1174–1186, 2014.

[12] A. M. Franz, T. Haidegger, W. Birkfellner, K. Cleary, T. M. Peters, and L. M. Hein, "Electromagnetic tracking in medicine-a review of technology, validation, and applications," *IEEE Trans. on Medical Imaging*, vol. 33, no. 8, pp. 1702–1724, 2014.

[13] T. Roberts, W. Hassenzahl, S. Hetts, and R. Arenson, "Remote control of catheter tip deflection: An opportunity for interventional mri," *Magn. Reson. Med.*, vol. 48, no. 6, pp. 1091–1095, 2002.

[14] F. Settecase, M. S. Sussman, M. W. Wilson, S. Hetts, R. L. Arenson, V. Malba, A. F. Bernhardt, W. Kucharczy, and T. P. L. Roberts, "Magnetically-assisted remote control (marc)steering of endovascular catheters for interventional mri: A model for deflection and design implications," *Med. Phys.*, vol. 34, no. 8, pp. 3135–3142, 2007.

[15] A. Krieger, I. I. Iordachita, P. Guion, A. K. Singh, A. Kaushal, C. Menard, P. A. Pinto, K. Camphausen, G. Fichtinger, and L. L. Whitcomb, "An mri-compatible robotic system with hybrid tracking for mri- guided prostate intervention," *IEEE Trans. on Biomedical Engineering*, vol. 58, no. 11, pp. 3049–3060, 2011.

[16] L. B. Kratchman, T. L. Bruns, J. J. Abbott, and R. J. W. III, "Guiding elastic rods with a robot-manipulated magnet for medical applications," *IEEE Trans. on Robotics*, vol. 33, no. 1, pp. 227–233, Feb. 2017.

[17] K. M. Popek, T. Schmid, and J. J. Abbott, "Six-degree-of-freedom localization of an untethered magnetic capsule using a single rotating magnetic dipole," *IEEE Robotics and Auto. Letters*, vol. 2, no. 1, pp. 305–312, 2017.

[18] C. D. Natali, M. Beccani, N. Simaan, and P. Valdastri, "Jacobian-based iterative method for magnetic localization in robotic capsule endoscopy," *IEEE Trans. on Robotics*, vol. 32, no. 2, pp. 327–338, Apr. 2016.

[19] C. D. Natali, M. Beccani, and P. Valdastri, "Real-time pose detection for magnetic medical devices," *IEEE Trans. on Magnetics*, vol. 49, no. 7, pp. 3524–3527, 2013.

[20] M. Beccani, C. Di Natali, L. J. Sliker, J. A. Schoen, M. E. Rentschler, and P. Valdastri, "Wireless tissue palpation for intraoperative detection of lumps in the soft tissue," *IEEE Trans. on Biomedical Engineering*, vol. 61, pp. 353–361, Feb 2014.

[21] K. Popek and J. Abbott, "6-d localization of a magnetic capsule endoscope using a stationary rotating magnetic dipole field," *Hamlyn Symp. Med. Robotics*, vol. 33, no. 8, pp. 47–48, 2015.

[22] H. Zhou, G. Alici, and F. Munoz, "A magnetically actuated anchoring system for a wireless endoscopic capsule," *Biomed Mircodevices*, vol. 18, no. 102, pp. 1–9, 2016.

[23] F. Munoz, G. Alici, W. Li, and M. Sitti, "Size optimization of a magnetic system for drug delivery with capsule robots," *IEEE Trans. on Magnetics*, vol. 52, no. 5, pp. 1–11, 2016.

[24] R. Ravaud and G. Lemarquand, "Analytical expression of the magnetic field created by tile permanent magnets tangentially magnetized and radial currents in massive disks," *Prog. Electromagn. Res. B*, vol. 13, no. 13, pp. 309–328, 2009.

[25] E. P. Furlani, "Formulas for the force and torque of axial couplings," *IEEE Trans. on Magnetics*, vol. 29, no. 5, pp. 2295 – 2301, 1993.

[26] D. Son, S. Yim, and M. Sitti, "A 5-d localization method for a magnetically manipulated untethered robot using a 2-d array of hall-effect sensors," *IEEE/ASME Trans. on Mechatronics*, vol. 21, no. 2, pp. 708–716, Apr. 2016.

[27] A. W. Mahoney and J. J. Abbott, "Generating rotating magnetic fields with a single permanent magnet for propulsion of untethered magnetic devices in a lumen," *IEEE Trans. on Robotics*, vol. 30, no. 2, pp. 411–420, Apr. 2014.

[28] F. Munoz, G. Alici, H. Zhou, W. Li, and M. Sitti, "Analysis of magnetic interaction in remotely controlled magnetic devices and its application to a capsule robot for drug delivery," *IEEE/ASME Trans. on Mechatronics*, vol. 23, no. 1, pp. 298–310, 2018.

[29] A. Z. Taddese, P. R. Slawinski, M. Pirotta, E. D. Momi, K. L. Obstein, and P. Valdastri, "Enhanced real-time pose estimation for closed-loop robotic manipulation of magnetically actuated capsule endoscopes," *Intl. Journal of Robotics Research*, vol. 37, no. 8, pp. 890–911, 2018.

[30] K. M. Popek, T. Hermans, and J. J. Abbott, "First demonstration of simultaneous localization and propulsion of a magnetic capsule in a llumen using a single rotating magnet," in *IEEE Intl. Conf. on Robotics and Automation*, pp. 1154–1160, May 2017.